Finite-Difference Time-Domain Modeling of Curved Surfaces

Thomas G. Jurgens, *Member, IEEE,* Allen Taflove, *Fellow, IEEE*
Korada Umashankar, *Senior Member, IEEE,* and
Thomas G. Moore, *Member, IEEE*

***Abstract*—In this paper the finite-difference time-domain (FDTD) method is generalized to include the accurate modeling of curved surfaces. This generalization, the contour path (CP) method, accurately models the illumination of bodies with curved surfaces, yet retains the ability to model corners and edges. CP modeling of two-dimensional electromagnetic wave scattering from objects of various shapes and compositions is presented.**

I. Introduction

A significant flaw in previous finite-difference time-domain (FDTD) models of structures with smooth curved surfaces has been to use stepped edge (staircase) approximations of the actual structure surface. Although not a serious problem for modeling wave penetration and scattering for low-Q metal cavities, recent FDTD studies have shown that stepped approximations of curved walls and aperture surfaces can shift center frequencies of resonant responses by 1 to 2% for Q factors of 30 to 80, and can possibly introduce spurious nulls [1]. In the area of scattering by complex shapes, the use of stepped surface approximations has limited the application of FDTD for the modeling of the important target class where surface roughness, exact curvature, and dielectric or permeable loading is important in determining the radar cross section. This paper reports on a generalization of the FDTD method, the contour path (CP) method, where grid cells local to structure surfaces are deformed.

Recently, three different types of FDTD conformable surface models have been proposed and examined for scattering problems.

1) *Locally distorted grid models.* These preserve the basic Cartesian grid arrangement of field components at all space cells except those immediately adjacent to the structure surface. Space cells adjacent to the structure surface are deformed to conform with the surface locus. Slightly modified time stepping expressions for the field components adjacent to the surface are obtained by applying either a modified finite volume technique [2] or the CP technique.

2) *Globally distorted grid models, body fitted.* These employ available numerical mesh generation schemes to construct non-Cartesian grids which are continuously and globally stretched to conform with smoothly shaped structures. In effect, the Cartesian grid is mapped to a numerically generated coordinate system wherein the structure surface contour occupies a locus of constant equivalent "radius." Time-stepping expressions are adapted either from the Cartesian FDTD case [3] or from a characteristics based method used in computational fluid dynamics [4].

3) *Globally distorted grid models, unstructured.* These employ available numerical mesh generation schemes to construct non-Cartesian grids comprised of an unstructured array of space filling cells. Structure surface features are appropriately fit into the unstructured grid, with local grid resolution and cell shape selected to provide the desired geometric modeling aspects. An example of this class is the control region approach discussed in [5].

Research is ongoing for each of these types of conformable surface models. Key questions concerning the usefulness of each model include the following:

1) computer resources involved in mesh generation;
2) severity of numerical artifacts introduced by grid distortion, which includes numerical instability, dispersion, and nonphysical wave reflection, and subtraction noise;
3) limitation of the near-field computational range due to subtraction noise;
4) comparative computer resources for running realistic scattering models, especially for three-dimensional targets spanning 10 wavelengths or more.

II. Review of the FDTD Method

In this section the analytical basis of the FDTD method will be briefly described first, since the CP method is a generalization of it. Detailed descriptions of the FDTD method can be found elsewhere [6]–[10].

The traditional FDTD algorithm is a direct solution of Maxwell's time dependent curl equations, which are shown in Table I(a). The algorithm applies a second-order accurate finite difference approximation to the space and time deriva-

Manuscript received October 20, 1989; revised September 30, 1991. The work of A. Taflove was supported in part by National Science Foundation Grant ASC-8811273, the Office of Naval Research under Contract N00014-88-K-0475, and General Dynamics P.O. 4059045.

T. G. Jurgens is with the Fermi National Accelerator Laboratory, Mail Stop 308, Batavia, IL 60510.

A. Taflove is with the Department of Electrical Engineering and Computer Science, McCormick School of Engineering, Northwestern University, Evanston, IL 60208.

K. Umashanker is with the Department of Electrical Engineering and Computer Science, University of Illinois, Chicago, IL 60680.

T. G. Moore is at the Massachusetts Institute of Technology Lincoln Laboratory, Boston, MA 02173.

IEEE Log Number 9106597.

TABLE I

(a) MAXWELL'S CURL EQUATIONS IN CARTESIAN COORDINATES

$$\frac{\partial H_x}{\partial t} = \frac{1}{\mu}\left(\frac{\partial E_y}{\partial z} - \frac{\partial E_z}{\partial y} - \rho' H_x\right) \tag{1}$$

$$\frac{\partial H_y}{\partial t} = \frac{1}{\mu}\left(\frac{\partial E_z}{\partial x} - \frac{\partial E_x}{\partial z} - \rho' H_y\right) \tag{2}$$

$$\frac{\partial H_z}{\partial t} = \frac{1}{\mu}\left(\frac{\partial E_x}{\partial y} - \frac{\partial E_y}{\partial x} - \rho' H_z\right) \tag{3}$$

$$\frac{\partial E_x}{\partial t} = \frac{1}{\epsilon}\left(\frac{\partial H_z}{\partial y} - \frac{\partial H_y}{\partial z} - \sigma E_x\right) \tag{4}$$

$$\frac{\partial E_y}{\partial t} = \frac{1}{\epsilon}\left(\frac{\partial H_x}{\partial z} - \frac{\partial H_z}{\partial x} - \sigma E_y\right) \tag{5}$$

$$\frac{\partial E_z}{\partial t} = \frac{1}{\epsilon}\left(\frac{\partial H_y}{\partial x} - \frac{\partial H_x}{\partial y} - \sigma E_z\right) \tag{6}$$

where

E_x, E_y, E_z	Cartesian components of electrical field, v/m
H_x, H_y, H_z	Cartesian components of magnetic field, v/m
ϵ	electric permittivity, F/m
σ	electric conductivity, S/m
μ	magnetic permeability, H/m
ρ'	equivalent magnetic loss, Ω/m

(b) CENTRAL DIFFERENCE APPROXIMATION TO SPACE AND TIME PARTIAL DERIVATIVES

$$(i, j, k) = (i\Delta x, j\Delta y, k\Delta z) \tag{7}$$

$$F^n(i, j, k) = F(i\Delta x, j\Delta y, k\Delta z, n\Delta t) \tag{8}$$

$$\frac{\partial F^n(i, j, k)}{\partial x} = \frac{F^n\left(i + \frac{1}{2}, j, k\right) - F^n\left(i - \frac{1}{2}, j, k\right)}{\Delta x} + \text{order}\,(\Delta x^2) \tag{9}$$

$$\frac{\partial F^n(i, j, k)}{\partial t} = \frac{F^{n+\frac{1}{2}}(i, j, k) - F^{n-\frac{1}{2}}(i, j, k)}{\Delta t} + \text{order}\,(\Delta t^2) \tag{10}$$

for a cubic space lattice, $\Delta x = \Delta y = \Delta z \equiv \delta$

TABLE II

EXAMPLES OF FINITE-DIFFERENCE EQUATIONS DERIVED FROM MAXWELL'S EQUATIONS

$$H_x^{n+\frac{1}{2}}(i, j + 1/2, k + 1/2) = H_x^{n-\frac{1}{2}}(i, j + 1/2, k + 1/2) + \frac{\Delta t}{\mu(i, j + 1/2, k + 1/2)}\left[\begin{array}{l} \frac{1}{\Delta z}\left(E_y^n\left(i, j + \frac{1}{2}, k + 1\right) - E_y^n\left(i, j + \frac{1}{2}, k\right)\right) \\ + \frac{1}{\Delta y}\left(E_z^n\left(i, j, k + \frac{1}{2}\right) - E_z^n\left(i, j + 1, k + \frac{1}{2}\right)\right) \end{array}\right] \tag{11}$$

$$E_z^{n+1}(i, j, k + 1/2) = \frac{1 - \frac{\sigma(i, j, k + 1/2)\Delta t}{2\epsilon(i, j, k + 1/2)}}{1 + \frac{\sigma(i, j, k + 1/2)\Delta t}{2\epsilon(i, j, k + 1/2)}} E_z^n(i, j, k + 1/2) + \frac{1}{1 + \frac{\sigma(i, j, k + 1/2)\Delta t}{2\epsilon(i, j, k + 1/2)}} \times \frac{\Delta t}{\epsilon(i, j, k + 1/2)}\left[\begin{array}{l} \frac{1}{\Delta x}\left(H_y^{n+\frac{1}{2}}\left(i + \frac{1}{2}, j, k + \frac{1}{2}\right) - H_y^{n+\frac{1}{2}}\left(i - \frac{1}{2}, j, k + \frac{1}{2}\right)\right) \\ + \frac{1}{\Delta y}\left(H_x^{n+\frac{1}{2}}\left(i, j, -\frac{1}{2}, k + \frac{1}{2}\right) - H_x^{n+\frac{1}{2}}\left(i, j + \frac{1}{2}, k + \frac{1}{2}\right)\right) \end{array}\right] \tag{12}$$

tives of each cartesian field component. These central difference approximations are displayed in Table I(b).

The above equations combined with the constitutive relations result in a set of difference equations, examples of which are given in Table II. The constitutive relations are:

$$\vec{D} = \epsilon \vec{E} \tag{13}$$

$$\vec{B} = \mu \vec{H} \tag{14}$$

$$\vec{J}_c = \sigma \vec{E} \tag{15}$$

where ϵ, μ, and σ are the permittivity, permeability, and coductivity, respectively. All quantities on the right-hand side of each difference equation are known from computations performed at previous time steps. This results in a fully explicit system of difference equations whereby chronological values of the electric and magnetic field components at each location are obtained in a temporal leapfrog manner. Spatially, the computations are dependent on nearby field components, which enhances the method's ability to be computed on parallel architecture machines [11]. Fig. 1(b) illustrates the resulting spatial relationship between the field components.

Now that the structure of an individual FDTD cell has been described, the structure of the complete FDTD lattice will be discussed. The lattice is partitioned into two volumes, a total field region and a scattered field region, as illustrated in Fig. 1(c). Inside the total field region both incident and scattered waves exist. This region also encompasses the entire scattering body. No boundary condition needs to be applied at the body's surface, the medium changes implicitly with the cell to cell change of material characteristics (σ, ϵ, μ). The overwhelming majority of lattice cells are in the total field region, a percentage that increases with the lattice size. The scattered field region surrounds the total field region. The scattered field region is necessary in order to utilize an accurate radiation boundary condition introduced by Mur [12]. The basis of this radiation condition is a two-term Taylor series approximation of a one-way wave equation [13]. The existence of a scattered field region also permits the implementation of a near- to far-field transformation [14], based upon the electromagnetic field equivalence principle [15].

At this point it is worthwhile to remark that some FDTD codes do not divide their lattices into total and scattered field regions explicitly. In these codes, only scattered fields exist external to an object, while total fields are in the interior. The incident field is introduced by applying an appropriate boundary condition on an object's surface. For example, a perfectly conducting body would have the condition $E_{\text{scat}} = -E_{\text{inc}}$ applied to E-field components tangent to the body's surface. This methodology becomes quite cumbersome for materially complex heterogeneous objects. In addition, these codes suffer from accuracy problems in modeling the interior of shielded cavities and shadow regions [16], [17].

III. Analytical Basis of the Contour Path Method

A. Introduction

The CP algorithm is based on Ampere's and Faraday's laws, shown below:

$$\oint_C \vec{H} \cdot d\vec{l} = \int\int_S (\vec{J}_c + \vec{J}_s) \cdot d\vec{S} + \frac{\partial}{\partial t} \int\int_S \vec{D} \cdot d\vec{S} \tag{16}$$

$$\oint_C \vec{E} \cdot d\vec{l} = -\frac{\partial}{\partial t} \int\int_S \vec{B} \cdot d\vec{S} \tag{17}$$

where $\vec{E}$, $\vec{D}$, $\vec{H}$, $\vec{B}$, $\vec{J}_s$ and $\vec{J}_c$ denote the electric field, electric flux density, magnetic field, magnetic flux density, conduction current and source current, respectively, and the C contours enclose the S surfaces. The contours of Ampere's and Faraday's laws intersect each other's enclosed surface in much the same way as the links in a chain intersect. Fig. 1(a) illustrates this relationship, where the coordinates (u, v, w) are any cyclical permutation of x, y, and z. Implementing (16), the value of the E_u field component at time step n is calculated from the two H_v and the two H_w field components at time step $n - 1/2$ and the value of the E_u component at time step $n - 1$. Then implementing (17), the value of H_w at time step $n + 1/2$ is calculated from the two E_u and E_v components at time step n and the value of H_w at time step $n - 1/2$. In this leap frog manner the CP algorithm progresses with its calculations. For contours not near a media interface, the contour shape is rectangular and the CP difference equations are identical to the traditional FDTD difference equations. For example, this is a CP Faraday difference equation not near a media interface:

$$\begin{aligned} H_x^{n+\frac{1}{2}}(i, j+1/2, k+1/2) &= H_x^{n-\frac{1}{2}}(i, j+1/2, k+1/2) \\ &+ \frac{\Delta t}{A\mu(i, j+1/2, k+1/2)} \\ &\times \begin{bmatrix} l_3 E_y^n(i, j+\frac{1}{2}, k+1) - l_1 E_y^n(i, j+\frac{1}{2}, k) \\ +l_4 E_z^n(i, j, k+\frac{1}{2}) - l_2 E_z^n(i, j+1, k+\frac{1}{2}) \end{bmatrix}. \end{aligned} \tag{18}$$

In this equation, $A = \Delta y \Delta z$, $l_1 = l_3 = \Delta z$ and $l_2 = l_4 = \Delta y$. Thus, this equation is identical to the FDTD equation (11). Consequently, the CP method need only be applied to cells near a material interface, with the traditional FDTD method applied to the remaining cells. The total field-scattered field lattice partition, the near- to far-field lattice truncation and the absorbing boundary condition are unaffected by this inclusion of CP cells in the traditional FDTD grid.

Both the CP and the traditional FDTD methods have the same capabilities regarding time stepping and waveform modeling. The results presented here are obtained by illuminating the objects with a step sinusoid and waiting for the fields to reach steady state. Subtraction noise problems have never been observed with the traditional FDTD methodology and do not occur with the CP method either.

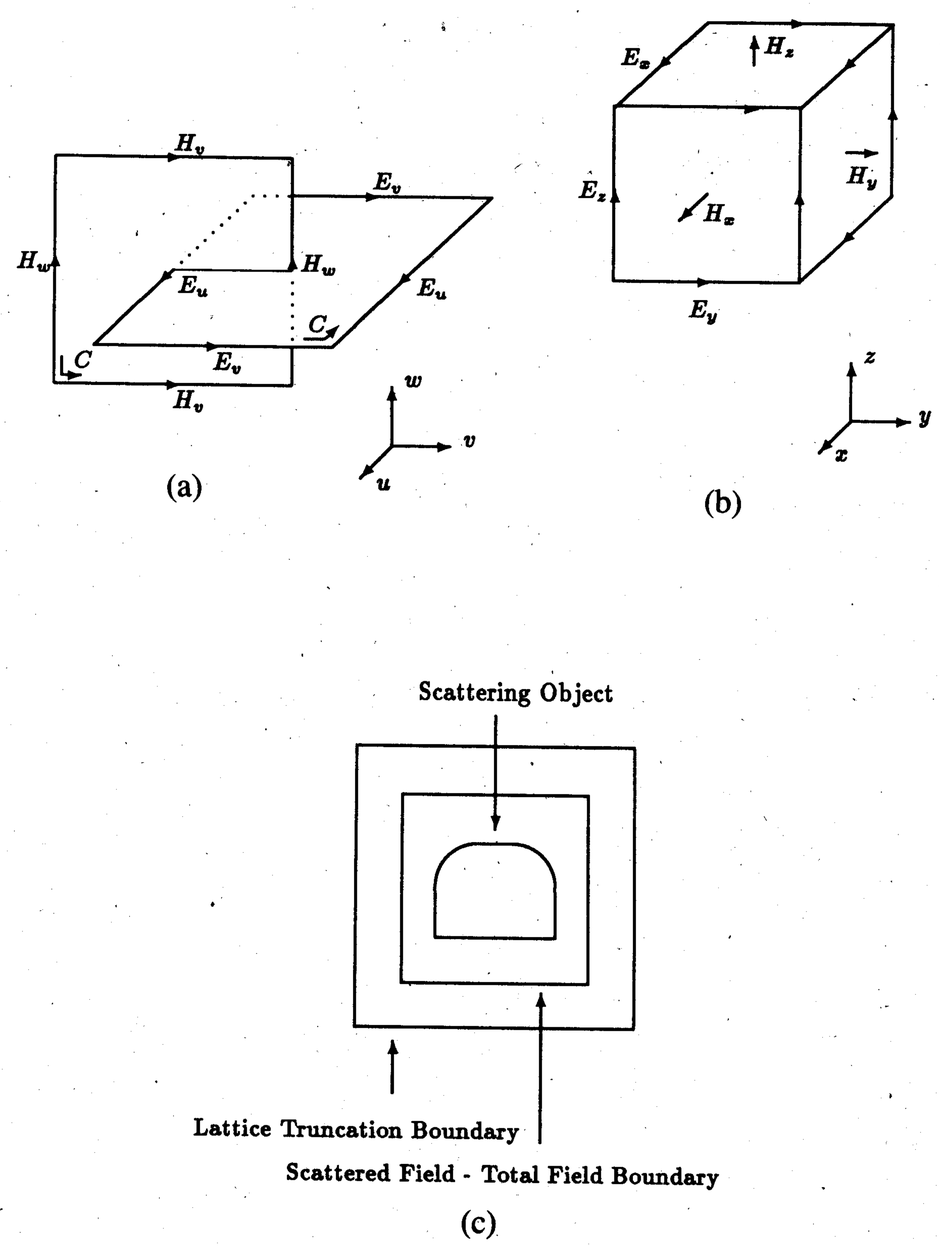

Fig. 1. (a) The CP Ampere and Faraday contour relationship. (b) A unit cell of the FDTD Lattice. (c) The FDTD lattice structure.

B. Perfectly Conducting Objects, TE Illumination

In this section the CP modeling of the TE illumination of perfectly conducting objects is discussed. First, the normally rectangular Faraday contours surrounding each H component near the object are deformed so as to conform to its surface. Each H component is assumed to represent the average value of the magnetic field within the patch bounded by the distorted contour. The electric field, $E_{\tan}$, on the distorted contour at the object surface is zero. Along the remaining straight portions of the contour, the electric field components are assumed to have no variation along their respective contour segments. Where possible these electric field components are calculated using rectangular Ampere contours from adjacent H components. The Ampere contours are not deformed. Also, calculations of Ampere contours which cross the media boundary are not used, necessitating that the E-field along the corresponding Faraday contour segments, if needed, are computed in some other way. These Faraday segments which intersect the object's surface, but are not tangent to it, have their E-field computed in one of two ways.

In the first way, the normal E approximation shown in Fig. 2(a), the projection onto the Faraday contour segment, of the E-field value at the intersection of the segment and the surface, is used. The E-field at this intersection point (E_n) is normal to the object's surface. E_n is calculated by setting up an auxiliary Ampere's law contour computation along the surface. The H-field values needed for the auxilary computation are interpolated from H-field components near the surface.

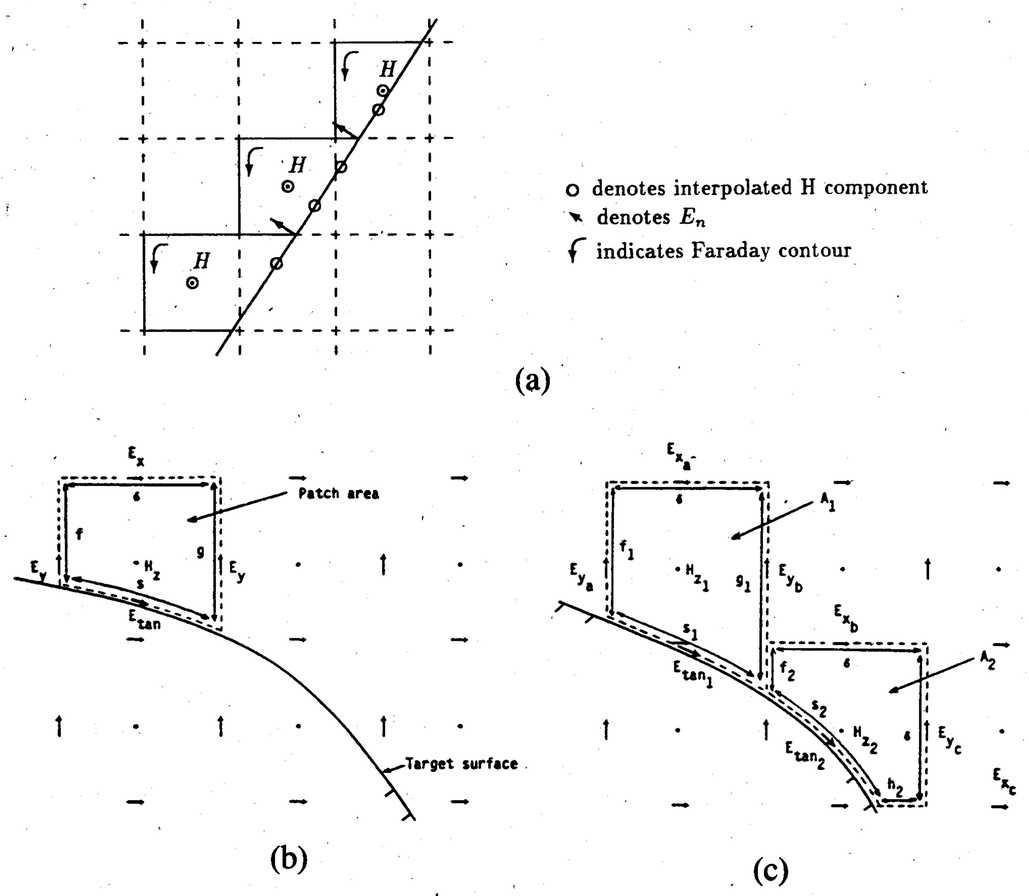

Fig. 2. CP TE methodology for perfectly conducting surfaces. (a) Normal E approximation. (b), (c) Nearest neighbor approximation.

The second way, the nearest neighbor approximation shown in Figs. 2(b) and 2(c), uses the near field component that is collinear with the Faraday contour segment, of the same type (E_x, E_y, etc.) and on the same side of the media interface as the Faraday segment. After applying Faraday's law for the three illustrative contours of Figs. 2(b) and 2(c), the following special FDTD time stepping relations are obtained for the H_z components immediately adjacent to the object surface, as listed below.

Standard Subcell – Fig. 2(b):

$$H_z^{n+\frac{1}{2}}(i+1/2, j+1/2) = C \cdot H_z^{n-\frac{1}{2}}(i+1/2, j+1/2) + D \cdot \left[E_y^n\left(i, j+\tfrac{1}{2}\right) \cdot f - E_y^n\left(i+1, j+\tfrac{1}{2}\right) \cdot g + E_x^n\left(i+\tfrac{1}{2}, j+1\right) \cdot \delta\right] \tag{19}$$

where

$$C = \left(\frac{\mu_0 A}{\delta t} - \frac{sZ_s}{2}\right) \Big/ \left(\frac{\mu_0 A}{\delta t} + \frac{sZ_s}{2}\right) \tag{20}$$

$$D = 1 \Big/ \left(\frac{\mu_0 A}{\delta t} + \frac{sZ_s}{2}\right). \tag{21}$$

Standard Stretched Cell – Fig. 2(c), component H_{z_1}:

$$H_{z_1}^{n+\frac{1}{2}}(i+1/2, j+1/2) = C_1 \cdot H_{z_1}^{n-\frac{1}{2}}(i+1/2, j+1/2) + D_1 \cdot \left[E_{y_a}^n\left(i, j+\tfrac{1}{2}\right) \cdot f_1 - E_{y_b}^n\left(i+1, j+\tfrac{1}{2}\right) \cdot g_1 + E_{x_a}^n\left(i+\tfrac{1}{2}, j+1\right) \cdot \delta\right] \tag{22}$$

where

$$C_1 = \left(\frac{\mu_0 A_1}{\delta t} - \frac{s_1 Z_{s_1}}{2}\right) \Big/ \left(\frac{\mu_0 A_1}{\delta t} + \frac{s_1 Z_{s_1}}{2}\right) \quad (23)$$

$$D_1 = 1 \Big/ \left(\frac{\mu_0 A_1}{\delta t} + \frac{s_1 Z_{s_1}}{2}\right). \quad (24)$$

Non-standard Subcell – Fig. 2(c), component H_{z_2}:

$$H_{z_2}^{n+\frac{1}{2}}(i+1/2, j+1/2) = C_2 \cdot H_{z_2}^{n-\frac{1}{2}}(i+1/2, j+1/2) + D_2 \cdot \left[\begin{array}{c} E_{y_b}^n\left(i, j+\frac{1}{2}\right) \cdot f_2 - E_{y_c}^n\left(i+1, j+\frac{1}{2}\right) \cdot \delta \\ + E_{x_b}^n\left(i+\frac{1}{2}, j+1\right) \cdot \delta - E_{x_c}^n\left(i+\frac{1}{2}, j+1\right) \cdot h_2 \end{array} \right] \quad (25)$$

where

$$C_2 = \left(\frac{\mu_0 A_2}{\delta t} - \frac{s_2 Z_{s_2}}{2}\right) \Big/ \left(\frac{\mu_0 A_2}{\delta t} + \frac{s_2 Z_{s_2}}{2}\right) \quad (26)$$

$$D_2 = 1 \Big/ \left(\frac{\mu_0 A_2}{\delta t} + \frac{s_2 Z_{s_2}}{2}\right). \quad (27)$$

In the above equations, we note that the only data needed to describe a distorted contour are:

1) the area of the patch, A, within the contour;
2) intercept points of the object surface contour with grid lines;
3) the subtended arc length, s, of the object surface;
4) knowledge of whether E components along the contour are calculable using the regular Yee algorithm; and
5) variation of the surface impedance, Z_s, with position along the object surface contour.

The distorted contour and field approximation information, obtained from a suitable geometry generation preprocessor, allows the CP code to the process the conformably modeled object surface contour as easily and quickly as the FDTD code, but with substantially better accuracy, as will be demonstrated shortly. However, the choice of the nearest neighbor or normal E approximations provide equal levels of accuracy. For completeness, we note that no magnetic or electric field components in the FDTD space lattice, other than the H_z components immediately adjacent to the object surface, require modified time stepping relations.

C. Perfectly Conducting Objects, TM Illumination

In the modeling of the TM illumination of perfectly conducting objects, the Faraday contours surrounding each H component located near the object are deformed so as to conform to its surface, as illustrated in Fig. 3. The Ampere contours are not deformed and calculations of Ampere contours which cross the media boundary are not used. Each such magnetic field component is assumed to represent the average value of the magnetic field within the patch bounded by the truncated contour. Z_s is the surface impedance of the object. The electric field, $E_{\tan}$, located on the truncated contour at the object's surface, is equal to Z_s times the local azimuthal magnetic field, H_ϕ. H_ϕ is collocated with $E_{\tan}$ and is obtained by interpolating the known H_x and H_y

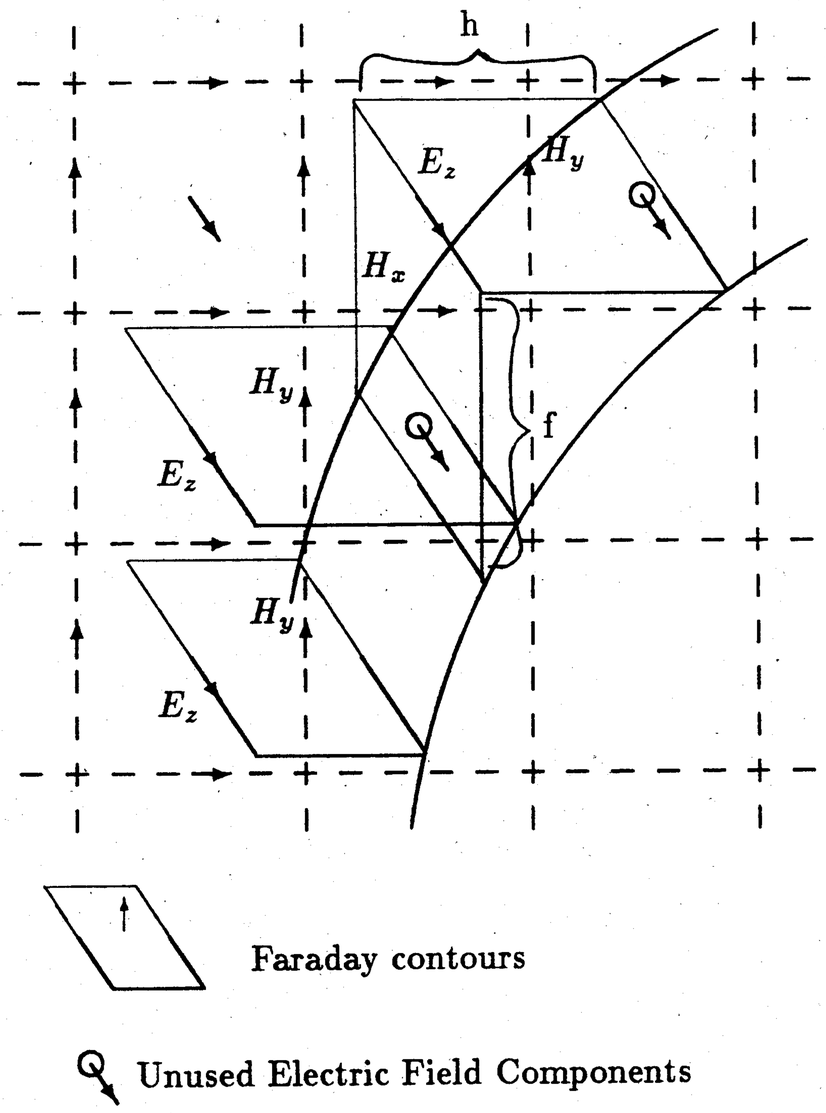

Fig. 3. Examples of modified Faraday's Law contour paths for the TM curved object.

components at this location and then adding their projections in the tangent direction.

For this study, consider only the case of $Z_s = 0$ (perfectly conducting object). This eliminates the need to calculate a local surface azimuthal magnetic field via interpolation and vectorial addition. Then, applying Faraday's law to the contours of Fig. 3,

$$H_x^{n+\frac{1}{2}}(i, j+1/2) = H_x^{n-\frac{1}{2}}(i, j+1/2) - \frac{\delta t}{\mu_0 f} \cdot E_z^n(i, j+1) \quad (28)$$

$$H_y^{n+\frac{1}{2}}(i+1/2, j) = H_y^{n-\frac{1}{2}}(i+1/2, j) + \frac{\delta t}{\mu_0 h} \cdot E_z^n(i, j) \quad (29)$$

where it is noted that the E_z component at the object surface is zero. Here, only the intercept point of the object surface contour with the gird lines need to be known. This is substantially less geometry data needed than for the TE illumination cases discussed earlier. The Faraday segments which lie along the object's surface are assigned an E-field value of zero, since the tangential electric field at a perfect conductor's surface is zero.

D. Dielectric Objects

For the modeling of dielectric objects, Faraday contours are deformed while the Ampere contours are not. Referring to Fig. 4, the Faraday contours are distorted so as to have them conform to the object's surface. Each H component is assumed to represent the average value of the magnetic field within the patch bounded by the distorted contour. The electric field, $E_{\tan}$, on the distorted contour at the object surface is calculated via an auxillary Ampere contour. Along

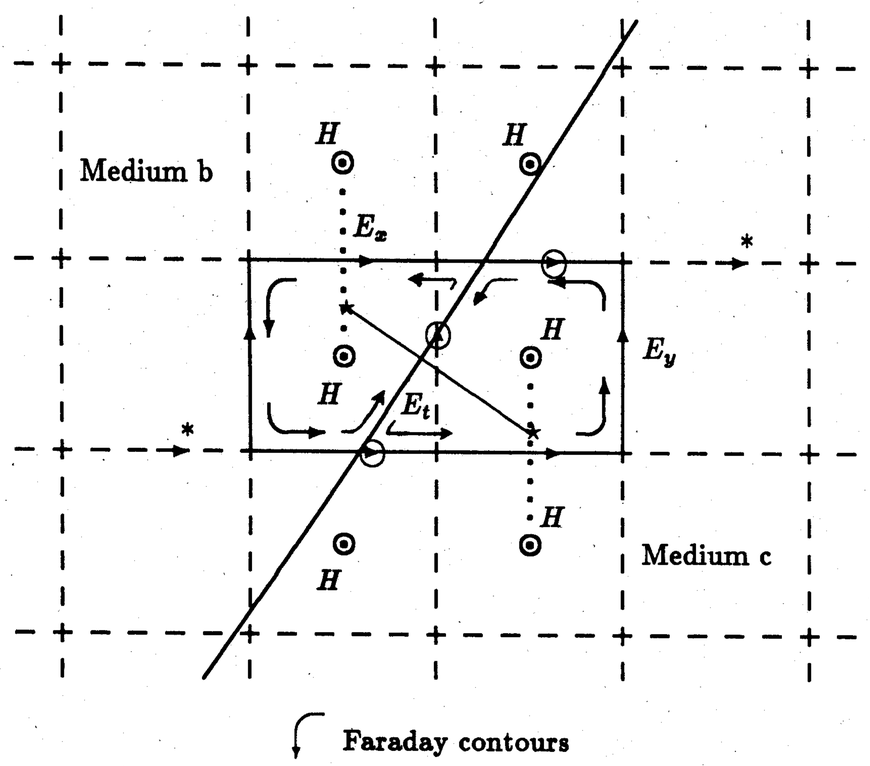

Fig. 4. Contour path TE Tangential E-field approximation for dielectric objects.

the remaining straight portions of the contour, the electric field components are assumed to have no variation along their respective contour segments. Where possible these electric field components are calculated using rectangular Ampere contours from adjacent H components. Also, calculations of Ampere contours which cross the media boundary are not used, necessitating that the E-field along the corresponding Faraday contour segments, if needed, is computed using the nearest neighbor approximation, as described above.

The Faraday's law difference equation for contours near the surface is:

$$H^{n+\frac{1}{2}}(i+1/2, j+1/2) = H_{z_2}^{n-\frac{1}{2}}(i+1/2, j+1/2) + D \cdot \begin{bmatrix} E_y^n(i, j+\frac{1}{2})\delta y - E_t^n(p) \cdot l_t \\ +E_x^n(i+\frac{1}{2}, j+1) \cdot l_3 - E_x^n(i+\frac{1}{2}, j) \cdot l_1 \end{bmatrix} \quad (30)$$

where

$$D = \frac{\delta t}{\mu_0 \mu_{\text{rel}} A} \quad (31)$$

and l_t is the length of the contour segment along the media interface, l_1 and l_3 are the lengths of the bottom and top contour segments, δy is the length of the left contour segment and p is the $E_{\tan}$ index.

The Ampere's law difference equation for the auxiliary tangential E-field components is:

$$E_t^{n+1}(p) = E_t^n(p) + \delta t \times \begin{bmatrix} \left(b_1 \cdot H^{n+\frac{1}{2}}(i+\frac{1}{2}, j+1\frac{1}{2}) + b_2 \cdot H^{n+\frac{1}{2}}(i+\frac{1}{2}, j+\frac{1}{2})\right)/A_b \epsilon_b (i+\frac{1}{2}, j) - \\ \left(c_1 \cdot H^{n+\frac{1}{2}}(i+1\frac{1}{2}, j+\frac{1}{2}) + c_2 \cdot H^{n+\frac{1}{2}}(i+1\frac{1}{2}, j-\frac{1}{2})\right)/A_c \epsilon_c (i+1\frac{1}{2}, j) \end{bmatrix} \quad (32)$$

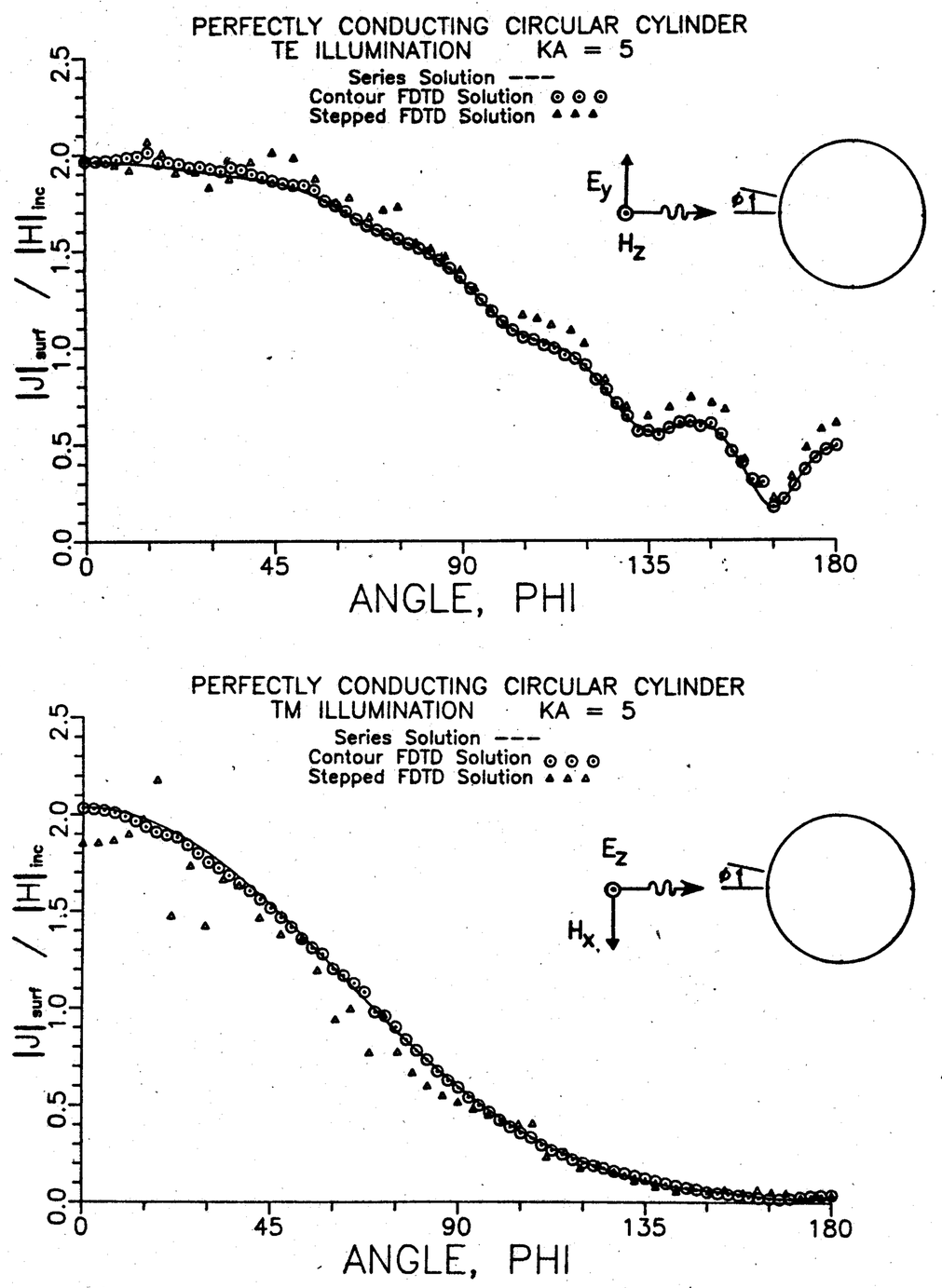

Fig. 5. Comparison of traditional FDTD, contour FDTD, and exact summed eigenseries solutions for surface current induced on a circular conducting cylinder. (a) TE illumination. (b) TM illumination ($\delta x = \lambda_0/20$ resolution).

where A_b and A_c are areas of the left and right portion of the Ampere's contour, respectively, and b_1, b_2, c_1 and c_2 are the coefficients for the H-field linear interpolation.

For the CP modeling of dielectric objects, TM illumination is the dual of TE illumination. That is, switching the roles of the magnetic field and the electric field, the permeability, μ, and the permittivity, ϵ, and the magnetic current and the electric current means that solving a TE illumination problem automatically provides data for a dual TM illumination problem.

E. Anisotropic Objects

The CP modeling of anisotropic dielectric objects is a direct extension of isotropic dielectric objects. For axially anisotropic dielectric media the relationship between the $\vec{D}$ and $\vec{E}$ fields is

$$\vec{D} = \begin{pmatrix} \epsilon_{xx} & 0 \\ 0 & \epsilon_{yy} \end{pmatrix} \vec{E}. \quad (33)$$

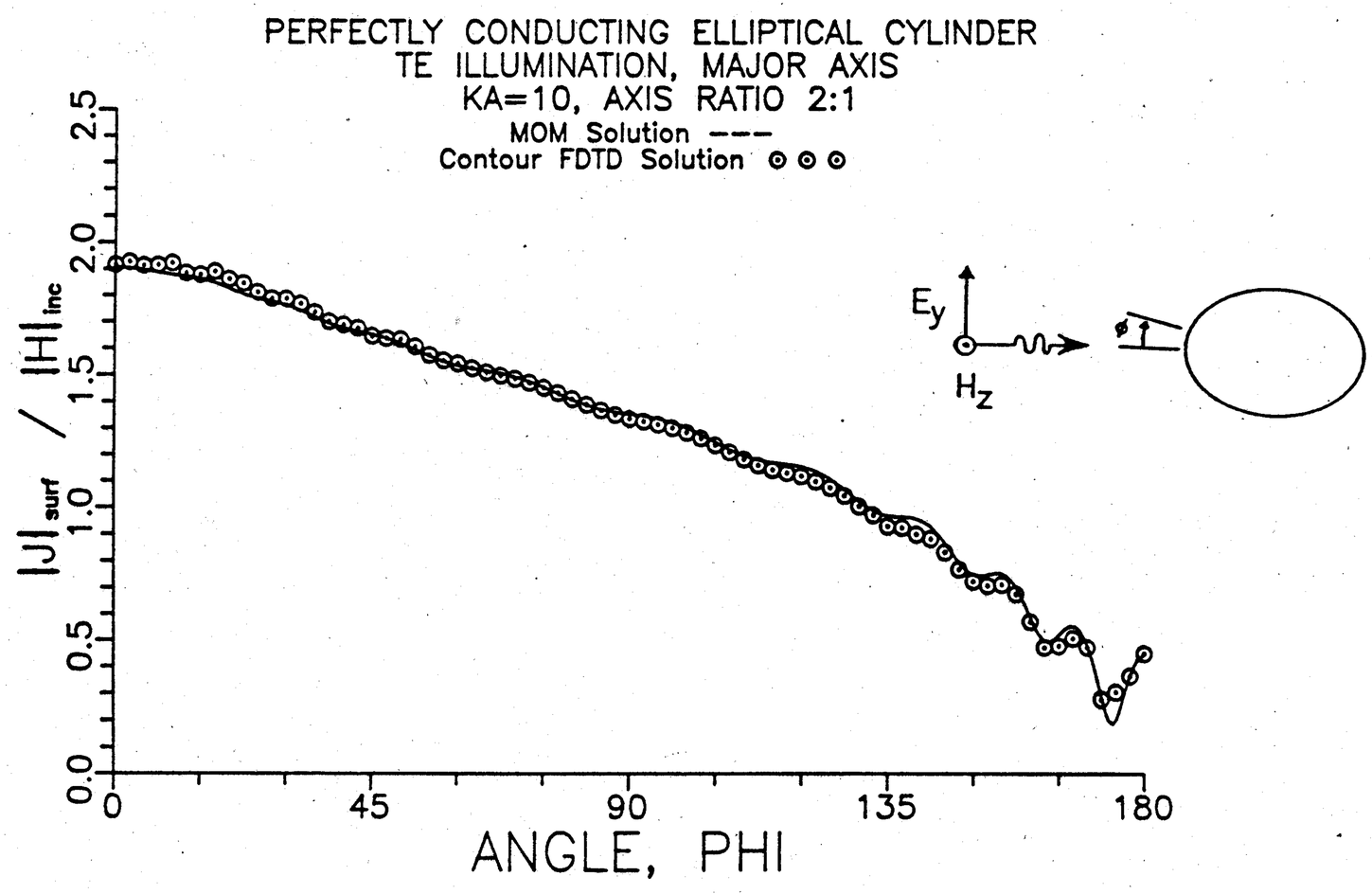

Fig. 6. Comparison of contour FDTD and method of moments solutions for surface current induced on an elliptical conducting cylinder, TE illumination ($\delta x = \lambda_0/20$ resolution).

This tensor relationship results in an Ampere's law difference equation which is a slight modification of (32).

$$E_t^{n+1}(p) = E_t^n(p) + \delta t \times \left[\begin{array}{c} \left(b_1 \cdot H^{n+\frac{1}{2}}\left(i+\frac{1}{2}, j+1\frac{1}{2}\right) + b_2 \cdot H^{n+\frac{1}{2}}\left(i+\frac{1}{2}, j+\frac{1}{2}\right)\right)/A_b \epsilon_b\left(i+\frac{1}{2}, j\right) \\ -\left(c_1 \cdot H^{n+\frac{1}{2}}\left(i+1\frac{1}{2}, j+\frac{1}{2}\right) + c_2 \cdot H^{n+\frac{1}{2}}\left(i+1\frac{1}{2}, j-\frac{1}{2}\right)\right)/A_c K \end{array} \right] \tag{34}$$

where A_b and A_c are areas of the left and right portion of the Ampere's law contour, respectively, and b_1, b_2, c_1 and c_2 are the coefficients for the H-field linear interpolation, and

$$K = \epsilon_{xx} \cos^2 \phi + \epsilon_{yy} \sin^2 \phi \tag{35}$$

where ϕ is the angle $E_{\tan}$ makes with the positive x-axis. The Faraday's law difference equation for this case is identical to the isotropic case (30). As in the isotropic case, TM illumination is the dual of TE illumination.

IV. Numerical Results

In this section analytical and numerical data validations of the CP method are presented. Objects of various shapes and compositions are analyzed.

A. Perfectly Conducting Objects

The first shape considered is a $k_0 a = 5$ circular cylinder, subjected to TE and TM illumination. Fig. 5 is a plot of the CP predicted surface current and the traditional (stepped) FDTD predicted surface current compared to the series solution. The CP method achieves an accuracy of 1% or better at most surface points resulting in accurate modeling of the peak and null structure of the current distribution. This figure also shows that the CP method is a significant improvement over the traditional FDTD method.

The next shape considered is an elliptical cylinder, subjected to TE illumination along its major axis. The circumference of the cylinder is 10 wavelengths and its axis ratio is 2:1. Fig. 6 is a plot of the CP predicted surface current compared to the method of moments solution. Once again, the CP method achieves accurate modeling of the peak and null structure of the current distribution.

The final shapes in this category are wing-like bodies, depicted in Fig. 7. It consists of a 10 in × 12 in metal plate, having steeply sloped sides with a central six inch radius chamfer on one side and either flat on the other side or having a symmetrically positioned V-shaped vertical slot on the other side. The measured data to be presented are for these three dimensional shapes, while the numerical data (the CP method and method of moments) are for the two dimensional shapes which result from allowing the 12 in dimension to go to infinity. Fig. 8(a) shows the monostatic radar cross section of the plate with the flat side. It is illuminated with a 10 GHz TM polarized wave. Fig. 8(b) shows the monostatic radar cross section of the plate with the V-slotted side. It is illuminated with a 16 GHz TE polarized wave. There is generally good agreement between the three sets of RCS data. In the low RCS regime near grazing incidence Fig. 8(b) shows that the CP method provides substantially better agreement with the measurements than MM. The residual disagreement between the CP and measured data is a consequence of the difference between the idealized 2-D computational model and the actual 3-D physical measured target.

For a given grid density, the CP method permits an object to be modeled more accurately than the traditional FDTD

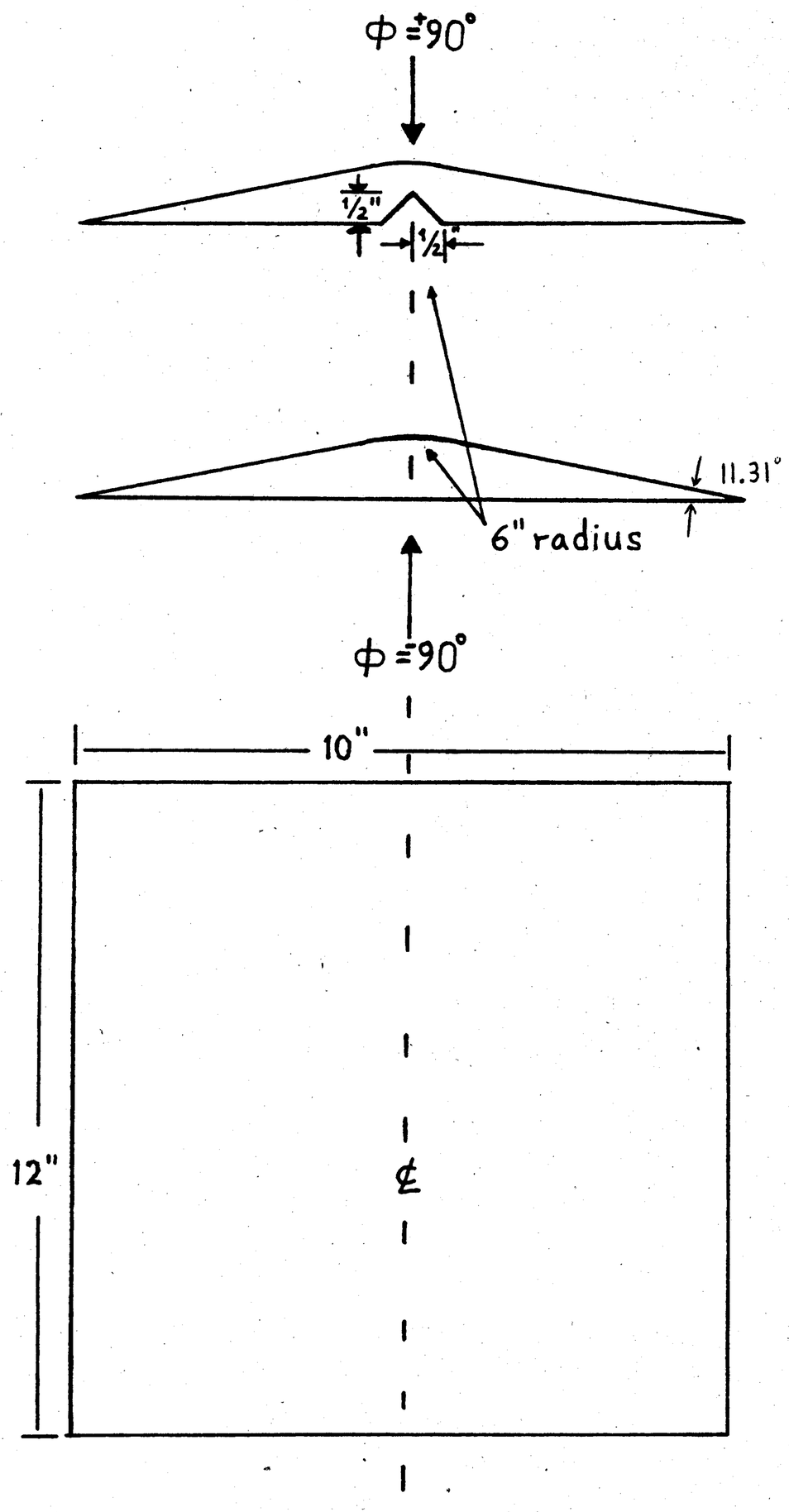

Fig. 7. Mechanical description of the wing-like body.

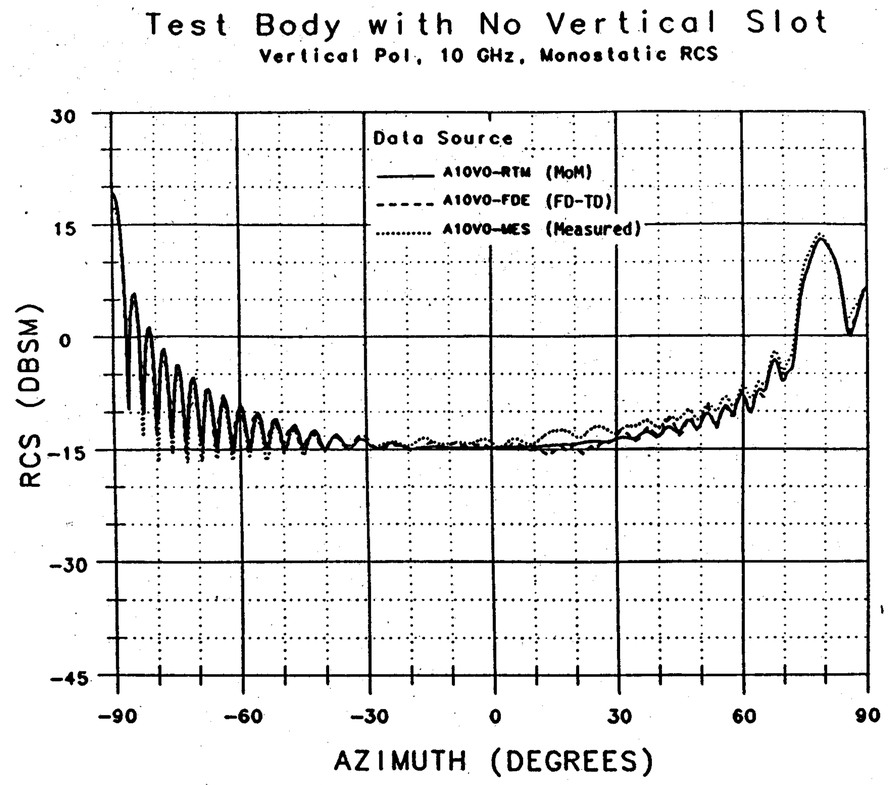

Fig. 8. Comparison of contour FDTD, method of moments and measured data for the radar cross section of a wing-like body. (a) TM illumination with no slot, (b) TE illumination with a V-shaped slot.

method. Both TE and TM cases are shown. Studies for the wing-like object indicate that $1/20\lambda_0$ gridding with CP surface modeling provides monostatic RCS accuracy better than with $1/80\lambda_0$ traditional (staircased) FDTD. This effect is most pronounced for incident angles near 90° as shown in Fig. 8(b). This is a *very large* advantage: in 2-D, more than 16:1 in storage and 64:1 in run time and in 3-D, more than 64:1 in storage and 256:1 in run time.

B. Dielectric Objects

The first shape considered is a TE illuminated $k_d a = 5$ circular cylinder, with $\epsilon_r = 4$. Fig. 9 is a plot of the CP predicted electric and magnetic surface current compared to the series solution. The CP method achieves an accuracy of 1% or better at most surface points resulting in accurate modeling of the peak and null structure of the current distributions.

The final shape in this category is a TE illuminated $k_0 a = 2.5$ anisotropic circular cylinder. The dielectric and magnetic coefficients for this object are $\epsilon_{xx} = 2\epsilon_0$, $\epsilon_{yy} = 4\epsilon_0$ and $\mu = 2\mu_0$. Fig. 10 is a plot of the CP predicted magnetic surface current compared to the combined field integral equation (CFIE) MM solution [18]. The CP method agrees with the MM results to 1% or better at most surface points resulting in accurate modeling of the peak and null structure of the current distributions.

V. Conclusion

This paper has introduced a generalization of the FDTD method, the contour path method. Examples of CP modeling of two dimensional electromagnetic wave scattering are presented. Objects of various shapes and compositions are analyzed. The method accurately models the illumination of bodies with curved surfaces, yet retains the ability to model corners and edges. The CP modeling of three-dimensional objects is presently being investigated.

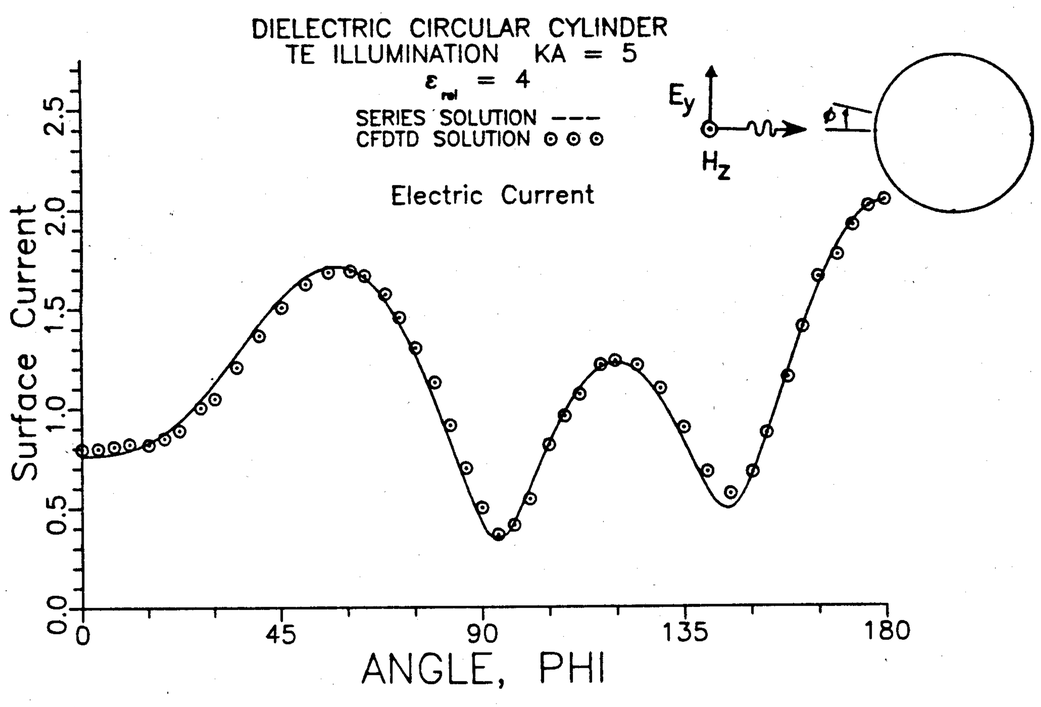

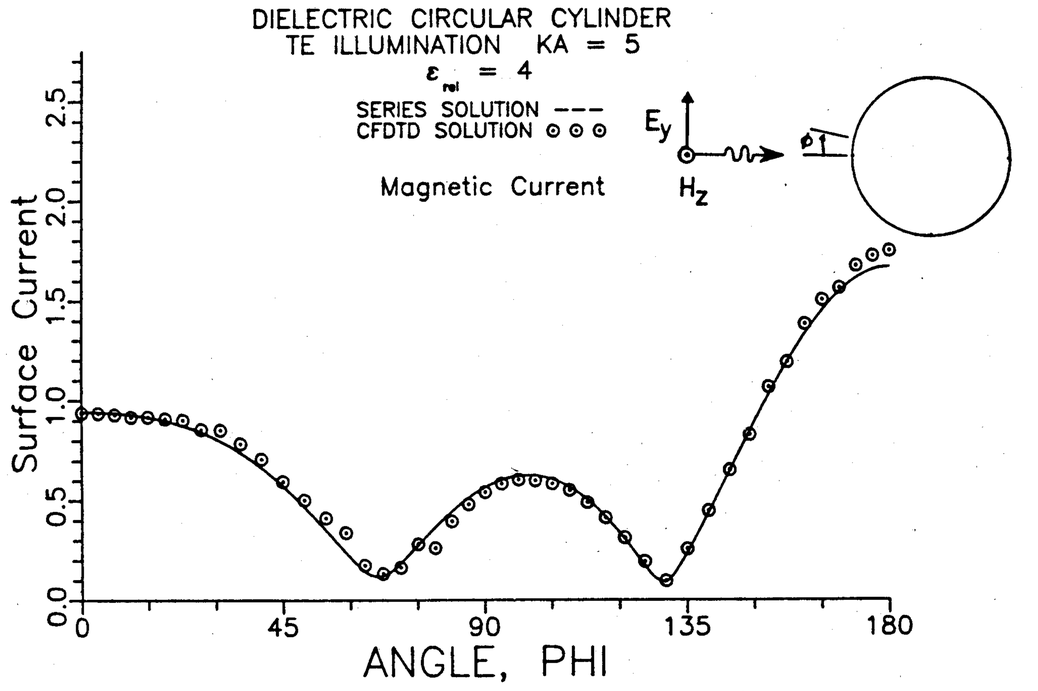

Fig. 9. Comparison of contour FDTD and exact summed eigenseries solutions for TE surface current induced on a dielectric circular cylinder. ($\delta x = \lambda_d/20$ resolution).

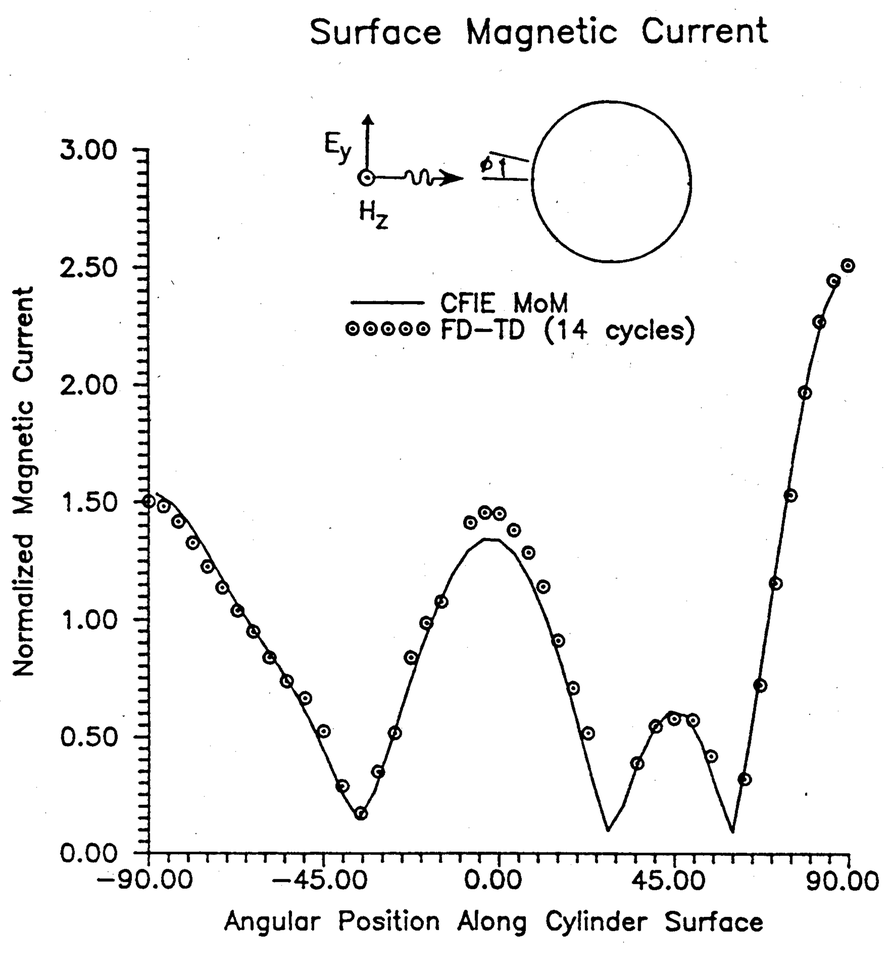

Fig. 10. Comparison of contour FDTD and method of moments solutions for TE surface current induced on an anisotropic circular cylinder with $\epsilon_{xx} = 2\epsilon_0$, $\epsilon_{yy} = 4\epsilon_0$ and $\mu = 2\mu_0$.

References

[1] K. R. Umashankar, A. Taflove, B. Beker, and K. Yee, "Calculation and experimental validation of induced currents on coupled wires in an arbitrary-shaped cavity," *IEEE Trans. Antennas Propagat.*, vol. AP-35, pp. 1248–1257, Nov. 1987.

[2] N. Madsen and R. Ziolkowski, "Numerical solution of Maxwell's equations in time domain using irregular nonorthogonal grids," *Wave Motion*, vol. 10, pp. 583–596, Dec. 1988.

[3] M. Fusco, "FDTD algorithm in curvilinear coordinates," *IEEE Trans. Antennas Propagat.*, vol. 38, pp. 76–89, Jan. 1990.

[4] V. Shankar, W. Hall, and A. H. Mohammadian, "A three-dimensional Maxwell's equation solver for computation of scattering from layered media," *IEEE Trans. Magn.*, vol. 25, pp. 3098–3103, July 1989.

[5] B. J. McCartin and J. F. DiCello, "Three-dimensional finite difference frequency domain scattering using the control region approximation," *IEEE Trans. Magn.*, vol. 25, pp. 3092–3094, July 1989.

[6] A. Taflove and K. R. Umashankar, "The finite difference time domain (FD-TD) method for electromagnetic scattering and interaction problems," *J. Electromagn. Waves Appl.*, 1(4):363–387, 1987.

[7] A. Taflove and K. Umashankar, "Radar cross section of general three-dimensional scatters. *IEEE Trans. Electromagn. Compat.*, vol. EMC-25, pp. 433–440, Nov. 1983.

[8] K. Umashankar and A. Taflove, "Analytical models for electromagnetic scattering," Hanscom Air Development Center, Hanscom AFB, MA, Tech. Rep., June 1984.

[9] A. Taflove, K. R. Umashankar, and T. G. Jurgens, "Validation of FD-TD modeling of the radar cross section of three-dimensional scatterers," *IEEE Trans. Antennas Propagat.*, vol. AP-33, pp. 662–666, June 1985.

[10] K. S. Yee, "Numerical solution of initial boundary value problems involving Maxwell's equations in isotropic media," *IEEE Trans. Antennas Propagat.*, vol. AP-14, pp. 302–307, May 1966.

[11] A. T. Perlik, T. Opashl, and A. Taflove, "Predicting scattering of electromagnetic fields using FDTD on a connection machine," *IEEE Trans. Magn.*, vol. 25, pp. 2910–2912, July 1989.

[12] G. Mur, "Absorbing boundary conditions for the finite-difference approximation of time-domain electromagnetic field equations," *IEEE Trans. Electromagn. Compat.*, vol. 23, pp. 377–382, Nov. 1981.

[13] T. G. Moore, J. G. Blaschak, G. A. Kriegsmann, and A. Taflove, "Theory and application of radiation boundary operators," *IEEE Trans. Antennas Propagat.*, vol. 36, pp. 1797–1812, Dec. 1988.

[14] K. R. Umashankar and A. Taflove, "A novel method to analyze electromagnetic scattering of complex objects," *IEEE Trans. Electromagn. Compat.*, vol. EMC-24, pp. 397–405, Nov. 1982.

[15] S. A. Schelkunoff, "Kirchoff formula, its vector analogue and other field equivalence theorems," *Comm. Pure Appl. Math.*, vol. 4, pp. 43–59, June 1951.

[16] A. Taflove, K. R. Umashankar, and T. G. Jurgens, "Comparative time and frequency domain solutions of Maxwell's equations for modeling radar cross section," in *Advances in Computer Methods for Partial Differential Equations - V*. June 1984, pp. 406–414.

[17] R. Holland and J. W. Williams, "Total field versus scattered field finite difference codes: a comparative assessment," *IEEE Trans. Nucl. Sci.*, vol. NS-30, pp. 4583–4588, Dec. 1983.

[18] B. Beker, K. R. Umashankar, and A. Taflove, "Numerical analysis and validation of the combined field surface integral equations for electromagnetic scattering by arbitrarily shaped two dimensional anisotropic objects," *IEEE Trans. Antennas Propagat.*, vol. 37, pp. 1573–1581, Dec. 1989.

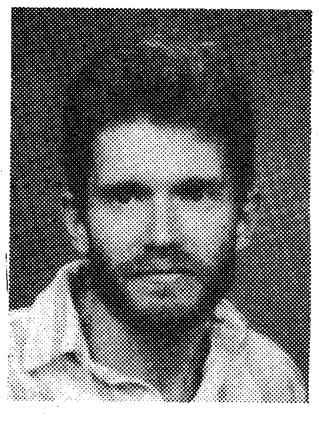

Thomas G. Jurgens (M'83) received the B.S.E.E. and M.S.E.E. degrees from the University of Illinois, Chicago, in 1980 and 1985, respectively, and the Ph.D. degree in electrical engineering from Northwestern University, Evanston, IL, in 1990.

He was with Northrop Corporation Rolling Meadows, IL from 1980–1982 and with IIT Research Institute from 1982–1985. From 1985 to 1987 he worked as a research assistant at Northwestern University. Since 1987 he has been at Fermi National Accelerator Laboratory, Batavia,

IL. His research activities have included the study of EMP interaction, electromagnetic scattering, particle accelerator field analysis and semiconductor device modeling.

Allen Taflove (M'75–SM'84–F'90), for a photograph and biography please see page 906 of the July 1991 issue of this TRANSACTIONS.

Korada Umashankar (S'69–M'75–SM'81), for a photograph and biography please see page 1212 of the August 1991 issue of this TRANSACTIONS.

Thomas G. Moore (S'84–M'89) received the B.S., M.S., and Ph.D. degrees from Northwestern University, Evanston, IL, in 1986, 1987, and 1989, respectively.

After receiving the Ph.D. degree, he joined the technical staff in the radar imaging group at MIT Lincoln Laboratory. While at Lincoln Laboratory he has worked on problems involving electromagnetic scattering and radar imaging. His research interests include computational electromagnetics, electromagnetic theory and nonlinear wave propagation.

Dr. Moore is a member of Tau Beta Pi and Eta Kappa Nu.